Tang et al. *NPG Asia Materials* (2024)16:16
https://doi.org/10.1038/s41427-024-00535-x

NPG Asia Materials

ARTICLE Open Access

Nanocomposite magnetic hydrogel with dual anisotropic properties induces osteogenesis through the NOTCH-dependent pathways

Shijia Tang[1,2,3], Yue Yan[1,2,3], Xiaoli Lu[1], Peng Wang[4], Xueqin Xu[5], Ke Hu[6], Sen Yan[7], Zhaobin Guo[8], Xiao Han[1,3], Feimin Zhang[1,2,3,6] and Ning Gu[6,7]

Abstract

Physical factors in the cellular microenvironment have critical effects on stem cell differentiation. The utilization of physical factors to promote the osteogenic differentiation of stem cells has been established as a new strategy for developing bone tissue engineering scaffolds. In this context, scaffolds with multiscale anisotropy are considered to possess biomimetic properties, which are advantageous for their biological performance. In the present study, a novel magnetic anisotropic hydrogel (MAH) with magnetic and topographic anisotropy was designed by combining static magnetic field-induced magnetic nanomaterials and a hydrogel. In in vitro studies, the MAH exhibited excellent biocompatibility and osteogenic bioactivity. The alkaline phosphatase activity and the expression of osteogenic-related genes and proteins induced by the MAH were greater than those induced by the pure PEGDA–GelMA hydrogel (PGH) and the magnetic isotropic hydrogel (MIH). In addition, the present study revealed that the dual anisotropic properties of the MAH activated the NOTCH1/2 pathway by upregulating SNHG5 and downstream SIRT6, which modulates the level of NOTCH1/2 by antagonizing DNMT1 protein stability, ultimately inducing the osteogenic differentiation of bone marrow mesenchymal stem cells (BMSCs). Furthermore, the MAH, MIH, and PGH were tested for in vivo bone regeneration in rabbits with femur defects, and the results demonstrated that the MAH effectively stimulated bone regeneration. Taken together, these findings suggest that this magnetically and topographically anisotropic biomimetic hydrogel might be a promising candidate for application in the field of bone tissue regeneration.

Introduction

Bone tissue engineering based on stem cells is a strategy for creating new functional bone structures by associating stem cells with scaffolds, which presents new opportunities for the reconstruction of bone defects and gaining new insights into pathologies[1,2]. Many studies have shown that soluble signaling molecules, such as differentiation-inducing chemicals, endothelial growth factor (VEGF), and bone morphogenetic proteins (BMPs), promote the osteogenesis of mesenchymal stem cells[3]. However, increasing evidence has revealed that stem cell differentiation is directly correlated not only with the chemical composition of the environment but also with the biophysical properties of the extracellular microenvironment, such as stiffness, shape, and topography[4]. Several studies have also shown that substrates with certain micro- or nanoscale topographical features promote the osteogenic differentiation of stem cells without the use of additional biological or chemical factors, thereby facilitating bone formation[5]. Moreover, a variety of biophysical factors may cooperatively regulate cell behaviors to achieve synergistic effects[6]. The ability of biophysical factors to guide the

Correspondence: Feimin Zhang (fmzhang@njmu.edu.cn)
[1]Jiangsu Province Key Laboratory of Oral Diseases, Nanjing Medical University, 210029 Nanjing, China
[2]Department of Prosthodontics, Affiliated Stomatological Hospital of Nanjing Medical University, 210029 Nanjing, China
Full list of author information is available at the end of the article

differentiation of stem cells makes the use of biophysical factors a promising approach for designing clinically applicable bone tissue engineering scaffolds with minimal need for chemical supplements. Tensile loading and dynamic mechanical stimulation have been reported to promote the osteogenic differentiation of stem cells and increase the expression of bone matrix proteins[7], and physical cues, such as microstructure, topography, and mechanical signals, can provide suitable niche features for osteogenesis and bone repair[8,9]. Furthermore, mechanical stimulation is an effective way to boost the osteogenic differentiation and extracellular matrix (ECM) production of cells in engineered bone constructs[10].

Numerous studies have shown that nanomaterial-based techniques are valuable tools for stimulating the differentiation of stem cells into osteoblasts and have potential applications in tissue engineering[11,12]. Many studies have shown that the combination of various nanomaterials with hydrogels can endow composite hydrogels with diverse physicochemical properties and biological functionalities[13–15]. This integration facilitates the creation of advanced biomaterials tailored for specific biomedical applications. Furthermore, magnetic nanomaterials (MNMs) have been shown to induce changes in intracellular calcium concentrations and mitogen-activated protein kinase activity in osteoblasts[16]. Magnetic stimulation is hypothesized to increase the osteogenic potential of stem cells and has potential applications in regenerative medicine. MNMs, such as iron oxide nanoparticles (IONPs), have been extensively demonstrated to promote bone regeneration and are used in many bone tissue engineering applications alone or in combination with a magnetic field[17]. The integration of MNMs into bone tissue engineering biomaterials has attracted great attention due to their potential to enhance mechanical properties and provide a local micromagnetic field that improves scaffold biological properties, such as osteointegration and osteoinduction[18,19]. At present, there are many methods for synthesizing biocompatible MNMA-based scaffolds, including in situ coprecipitation, sol–gel methods, electrospinning techniques, covalent assembly, and dipping[18,20]. However, most of the fabricated scaffolds are magnetically isotropic, and the magnetic moments of individual MNMs are relatively chaotic in most of these composites, reducing the efficiency of osteogenic induction and failing to maximize the magnetic biological effects of the MNMs. In addition, most magnetic composite scaffolds are assembled with MNMs on the surface of the scaffold, and the particles are easily dislodged in the cell culture environment, decreasing the stability of the assembled structure.

Human body tissues typically exhibit anisotropic structures on multiple scales, a product of the natural evolution of specific functions and properties. For instance, bone comprises highly ordered, interpenetrating networks of cross-linked collagen fibers within which hydroxyapatite nanocrystals are embedded[21]. The precise nanoscale arrangement of these anisotropic organic and inorganic phases endows bone tissue with unique mechanical properties and biological functionalities[22]. Studies have shown that anisotropically oriented matrices can promote the osteogenic differentiation of stem cells[23]. Chen et al.[24] coated type I collagen on PLGA/PCL electrospun fibers and found that fibers with an oriented anisotropic arrangement promoted the osteogenic differentiation of rat bone marrow mesenchymal stem cells more effectively than randomly oriented fibers. In another experiment, researchers fabricated a nanohydroxyapatite/polyamide scaffold with axial alignment and found that, compared to isotropic scaffolds, anisotropic scaffolds more effectively promoted new bone infiltration into the internal pores of the scaffold[25]. Moreover, in a rabbit calvarial defect repair experiment, the newly formed bone volume inside the anisotropic tissue engineering scaffold was significantly greater than that inside the isotropic scaffold. Anisotropic scaffolds could accelerate bone induction into non-load-bearing bone defect pores[26]. Growing evidence suggests that anisotropic scaffolds have broad application prospects in bone tissue engineering.

Polyethylene glycol diacrylate (PEGDA) is a derivative of polyethylene glycol (PEG) that is rapidly crosslinked under ultraviolet (UV) light when catalyzed by a photoinitiator. The resultant hydrogel has excellent hydrophilicity and elasticity and a tunable mechanical profile, and it forms a strong, rigid framework. Nevertheless, it does not provide adequate cell adhesion sites, which affects its ability to support cell attachment[27]. Different components can be mixed to adjust the physicochemical properties of hydrogels[28,29]. Methacrylated gelatin (GelMA) is a modified gelatin that can be crosslinked under UV and visible light using a photoinitiator. GelMA combines the attributes of both natural and synthetic biomaterials to provide a three-dimensional matrix that is ideal for cell proliferation and differentiation, along with outstanding biocompatibility and cellular responsiveness. Furthermore, the distinctive features of GelMA, including thermosensitivity, biodegradability, tunable mechanical strength, and the ability to facilitate bone differentiation and vascularization, make it a favorable choice in bone repair research. Hydrogels anchored in such polymer networks not only possess expedited shaping capabilities but also synergistically increase biocompatibility and mechanical resilience, which are advantageous properties in potential scaffold materials for bone tissue engineering[30–32].

In the present study, a new type of magnetic anisotropic hydrogel with both magnetic and topographic anisotropy was successfully fabricated based on the PEGDA–GelMA

hydrogel. Alkaline phosphatase (ALP) activity and the expression of osteogenic-related genes and proteins were measured to investigate the osteogenic bioactivity. Additionally, the osteogenic mechanism of the anisotropic magnetic and topographic hydrogels was investigated in this study. Moreover, the hydrogels were surgically implanted into rabbit condyle defects for in vivo bone regeneration assessment. Overall, we believe that this novel structure of the fabricated MAH induces the osteogenic differentiation of BMSCs and promotes osteogenesis.

Materials and methods

Fabrication of the magnetic hydrogel

The hydrogel prepolymerization solution was obtained by fully dissolving 15 wt% PEGDA, 5 wt% GelMA, 0.6 wt% N,N'-methylene-bis-acrylamide (MBA), and 1 wt% lithium phenyl-2,4,6-trimethylben-zoylphosphinate (LAP). The resulting solution was injected into a customized polytetrafluoroethylene mold and irradiated for 10 s using a light source with a wavelength of 405 nm to obtain a PEGDA–GelMA hydrogel (PGH). Maintaining the above ratios, PEGDA, GelMA, MBA, LAP, and PBS were added to a system containing a final concentration of 2 mg/mL γ-Fe_2O_3@PSC/PLL colloidal solution[33], and completely dissolved to obtain the magnetic hydrogel prepolymerization solution. To obtain the MAH, the mixture was then poured into the module and positioned at the midpoint between the poles of a pair of electromagnets, ensuring a relatively uniform magnetic field area during polymerization. The magnetic isotropic hydrogel (MIH) was fabricated via the same procedure but in the absence of a magnetic field. The PGH, MIH, and MAH were then sliced in parallel with the magnetic nanomaterial assemblies using customized modules, and the final sizes were determined according to different experimental requirements. The sliced hydrogel was dialyzed in ultrapure water for 2 days and sterilized with ethylene oxide before being used as a cell culture substrate.

Morphological observation of the magnetic hydrogel using scanning electron microscopy

From each set of gels, cross-sections were prepared in orientations both parallel and perpendicular to the longitudinal axis of the internal assembly. These specimens were strategically placed within the central active zone of the temperature-controlled holder and surrounded by a spread of frozen gel. Then, the temperature-controlled unit was activated to bring the temperature inside the sample cup down to approximately −25 °C, and the samples were subjected to scanning electron microscopy (SEM) to characterize their networks and inner assembly structures.

Ferromagnetic resonance (FMR) spectroscopy of magnetic hydrogel

Because the size of the hydrogel used for cell culture was too large for FMR spectroscopy, a small piece ($0.1 \times 0.5 \times 0.5\ cm^3$) was cut to match the detection requirements. The magnetic hydrogel was analyzed under the following two conditions: with the long axis of the internal anisotropic structure of the hydrogel parallel to the direction of the FMR magnetic field, and perpendicular to the direction of the magnetic field. Finally, the FMR spectrum curves were obtained and summarized in the same coordinate system for comparison.

Superconducting quantum interference device (SQUID) analysis of magnetic hydrogel

The water in the magnetic hydrogel was removed through the ethanol gradient dehydration method. The dehydrated magnetic hydrogel was analyzed under the following two conditions under a SQUID magnetic field: with the long axis of the anisotropic structure inside the hydrogel parallel to the direction of the magnetic field and perpendicular to the direction of the magnetic field. Finally, the SQUID analysis results for each sample were obtained, and their respective M–H curves were constructed.

Characterization of the mechanical properties of hydrogels

For the compressive mechanical test, hydrogels were produced in a cylindrical shape with a height of 10 mm and a diameter of 8 mm. Compression tests were conducted at room temperature utilizing a universal testing machine fitted with a 2 kN sensor. For each specimen, a stress–strain curve was plotted, and the peak fracture point was identified and used to derive the corresponding strain values. Young's modulus was the approximated linear fitting value in the initial linear part of the curve. The formula for calculating the Young's modulus is given by $E = \Delta\text{Stress}/\Delta\text{Strain}$ (where E is the Young's modulus, ΔStress is the applied force per unit area, and ΔStrain is the resulting deformation in length relative to the original length). The energy dissipation of the hydrogels was obtained by calculating the area of compression–relaxation cycles, in which the rate of compression was maintained at 2 mm/min. In the stress relaxation test, the strain for each compression process was set to 10%, and the process was repeated 5 times as previously described[34]. All tests were performed with three replicates.

Cell culture and transfection

MAH, MIH, and PGH samples were placed in separate wells of 12-well plates, and 1 mL of complete medium was added to each well for preculture. Human bone mesenchymal stem cells (BMSCs) were cultured in a

human mesenchymal stem cell basal medium supplemented with 10% fetal bovine serum and 1% penicillin–streptomycin. The cells were incubated in a humidified incubator at 37 °C in the presence of 5% CO_2. When the cell density reached ~80–90%, the cells were trypsinized to form suspensions with a concentration of 2×10^5 cells/mL. Then, 20 μL of cell suspension was seeded into each hydrogel sample (4000 cells/well), and the culture medium was changed every 2 days. The morphology of the BMSCs was observed by an inverted microscope (Leica DMC2900, Germany) using a bright field and then imaged using AxioVision Rel. 4.5 software. Short hairpin RNAs (Table S1) were synthesized by GenePharma (Shanghai, China). Cells in six-well plates were treated with 50 nM siRNAs or 4 mg of shRNAs using Lipofectamine 3000 reagent (Invitrogen, Carlsbad, CA, USA) according to the manufacturer's instructions and then harvested for assays.

Cell morphology observation and immunofluorescence (IF) staining

The morphology of BMSCs cultured on the MAH, MIH, and PGH was observed via confocal laser scanning microscopy (Zeiss-LSM710; Carl Zeiss Meditec AG, Jena, Germany) 48 h after cell seeding. The cells were washed twice with PBS and incubated with phalloidin and 4′,6-diamidino-2-phenylindole (DAPI) in the dark.

After 4 days of osteogenic differentiation, an IF staining assay was performed to measure the expression of RUNX2 in BMSCs cultured on MAH, MIH, and PGH. Briefly, cells were fixed with 4% paraformaldehyde at 4 °C, permeabilized with 0.5% Triton X-100, washed three times in PBS, and blocked with 3% BSA. The cells were then incubated overnight at 4 °C with diluted anti-RUNX2 primary antibody (1:6400, CST). The cells were then washed three times with PBST (PBS + 0.1% Tween 20) and further incubated with an Alexa Fluor 565-conjugated secondary antibody for 1 h at room temperature in the dark. Fluorescence images were obtained under a confocal microscope.

ALP activity assay

BMSCs were seeded as described above. After the cells were incubated in an osteogenic induction medium for 4 or 7 days, an ALP/AKP Assay Kit (Boqiao Biotech, Nanjing, China) and a BCIP/NBT ALP Color Development Kit (Beyotime, Shanghai, China) were used to evaluate ALP activity. The ALP activity and total protein concentration were determined and the ALP concentration was calculated according to the manufacturer's instructions for the corresponding kit.

RNA isolation and quantitative real-time polymerase chain reaction (qRT–PCR)

Total RNA was extracted from cells using TRIzol (Invitrogen, Carlsbad, CA, USA). Nuclear and cytoplasmic RNA was isolated from each fraction using a Nuclear/Cytosol Fractionation Kit (BioVision, San Francisco, CA, USA) following the manufacturer's instructions. The primer sequences are listed in Table S2. qRT–PCR was subsequently conducted using a QuantStudio 7 Flex (Applied Biosystems, Foster City, CA, USA) according to the manufacturer's instructions[35]. The $2^{-\Delta\Delta Ct}$ method was used to analyze the data. All the samples were analyzed in triplicate.

Western blot analyses

Western blotting was performed as previously described[35] using the following primary antibodies: BMP2, OCN, COLI, ALP, SIRT6, NOCTH1, NOCTH2, DNMT1, TUBLIUN, β-actin and GAPDH (Abcam, England).

RNA sequencing and data analysis

RNA was extracted from MAH- and MIH-cultured cells using TRIzol (Life Technologies, USA) and purified using an RNeasy Mini Kit (Qiagen, Germany). RNA-seq libraries were prepared using the Illumina TruSeq RNA Library Prep Kit v2 and sequenced with a HiSeq 2500 sequencer as previously described[33].

Luciferase reporter assay

The binding sites of miR-32 on SNHG5 and SIRT6 were predicted through bioinformatics websites. The 3'-UTR fragments of SNHG5 and SIRT6 that interact with miR-32 were cloned and inserted into pMIR-REPORT vectors. Cells were cotransfected with the miR-32 mimic or with related miRNAs and reporter constructs. Subsequently, luciferase activity was measured using a Dual-Luciferase Reporter Assay System (Promega, WI, USA) according to the manufacturer's instructions.

Fluorescence in situ hybridization (FISH)

FISH assays were performed with a FISH Kit (GenePharma, Shanghai, China; Cat. no. F11202) according to the manufacturer's instructions. The probe used in this study was synthesized and purchased from GenePharma (Shanghai, China). The cells were fixed in 4% paraformaldehyde for 20 min, preincubated, and then incubated with PBS and hybridization solution at 37 °C for 30 min. The cell nuclei were stained with DAPI, and images were acquired using a fluorescence microscope[36].

RNA pull-down assay

Biotinylated miRNA and the corresponding mutant/negative control were synthesized and purchased from GenePharma (Shanghai, China). The oligonucleotides were transfected into cells using Lipofectamine 3000 (Invitrogen, USA). After 48 h, the cell lysates were incubated with M-280 streptavidin magnetic beads (Invitrogen, USA). The expression of SNHG5 was measured by qRT–PCR.

Coimmunoprecipitation

Cells were lysed with NP-40 lysis buffer containing a protease inhibitor cocktail (Roche, Basel, Switzerland), and the immunoprecipitated complexes were recovered with ChIP grade antibodies against acetylated lysine (Ac-K) (Cell Signaling Technology, Danvers, MA, USA), the Flag epitope (Beyotime, Shanghai, China) and rabbit immunoglobulin (Ig)G control antibodies (Sigma-Aldrich, St. Louis, MO, USA), which were incubated with protein A/G Sepharose beads (Santa Cruz, CA, USA) and then rinsed with wash buffer. The eluted immune complexes were denatured and subjected to western blot analysis[37].

Femur condyle defect modeling

A total of 12 male New Zealand rabbits weighing 3–3.5 kg were chosen for the in vivo study. A defect 5 mm in diameter and 5 mm in depth was created in the lateral femur of comatose rabbits under anesthesia comprising lidocaine and propofol. The rabbits were randomized into four groups: the control group (no implantation of any material in the defect area), the PGH group (PGH was implanted in the defect area), the MIH group (MIH was implanted in the defect area), and the MAH group (MAH was implanted in the defect area) ($n = 6$ defects in each group). Penicillin was intramuscularly injected 3 days after the operation to prevent infection. The animals were sacrificed at 8 weeks after surgery to obtain the femur condyles for evaluating osteogenic activity.

Micro-CT analysis

The harvested femur samples were fixed in 4% paraformaldehyde for 3 days prior to micro-CT scanning (Bruettisellen, Switzerland). 3D reconstructions of the surgical area, which contained the scaffold and the newborn bone, were obtained with MIMICS 19.0 software. The percent bone volume (BV/TV), bone surface density (BS/TV), trabecular thickness (Tb.Th), trabecular separation (Tb.Sp), and trabecular number (Tb.N) were subsequently calculated.

Histological analysis

The samples used for the histological test were fixed with formalin at 4 °C for 24 h, decalcified with 15% ethylenediaminetetraacetic acid (EDTA) for 28 days, and dehydrated through a graded alcohol series. Subsequently, the samples were rinsed with deionized water, cleared in xylene, and embedded in paraffin, followed by sectioning at 5 μm. The sections were then stained with H&E or Masson's trichrome stain and observed under a microscope.

Statistical analyses

SPSS 23 software (IBM, USA) was used for statistical analysis. Differences between two groups of data were analyzed by an independent sample *t*-test, and differences between three or more groups were analyzed by ANOVA and Tukey post hoc analysis. $p < 0.05$ was considered to indicate statistical significance.

Results

Characterization of MAH and MIH

The magnetic anisotropic hydrogel (MAH) was fabricated by combining γ-Fe_2O_3@PSC/PLL (Fig. S1) and PEGDA–GelMA hydrogel with the assistance of a static magnetic field, while no magnetic field was applied in the fabrication of the corresponding magnetic isotropic hydrogel (MIH) (Fig. 1A). By adjusting the magnetic induction strength and duration of the applied magnetic field, we sought to identify the optimal assembly parameters to ensure a relatively uniform assembly structure within the hydrogel. Ultimately, we opted for an assembly time of 5 s and a magnetic induction intensity of 45 mT for the preparation of the MAH (Fig. S2). Many stripe-like structures oriented in the same direction were observed in the MAH under optical microscopy, while scattered dot-like structures were observed in the MIH (Fig. 1B). Scanning electron microscopy was used to examine cross-sections of the magnetic hydrogels both parallel and perpendicular to the assembly chain direction. In the SEM images, the MAH group displayed orientation along the assembly chain direction when cut parallel, whereas the MIH exhibited a more porous structure (Fig. 1C). When cut perpendicular to the assembly chain direction, the cross-section of the MAH revealed more uniformly aligned channels, in contrast to those of the MIH, which exhibited a structure similar to that observed in the parallel cut (Fig. 1D). This result confirmed the anisotropic network structure in the MAH and the isotropic structure in the MIH.

After immersion and preincubation in a cell culture medium for 7 days, the magnetic properties of the MAH and MIH were evaluated via SQUID and FMR spectroscopy experiments. According to the SQUID results, the *M*–*H* curves measured in both test directions largely overlapped for the MIH. A slight discrepancy between the two directions was observed in the *M*–*H* curves of the MAH, but the difference was not pronounced. We speculate that this result might be due to the dehydration process required for the SQUID test. Following dehydration, the oriented polymer network and assembly structures within the hydrogel could collapse and deform. Thus, FMR, a method that does not necessitate sample dehydration, was used for further research (Fig. 2A–C). For the MIH, the differences between the FMR spectra obtained under the two test conditions were negligible, and the *g*-factor difference was close to 0, demonstrating that the material had no magnetic anisotropy. In contrast, for the MAH, the differences between the FMR spectra

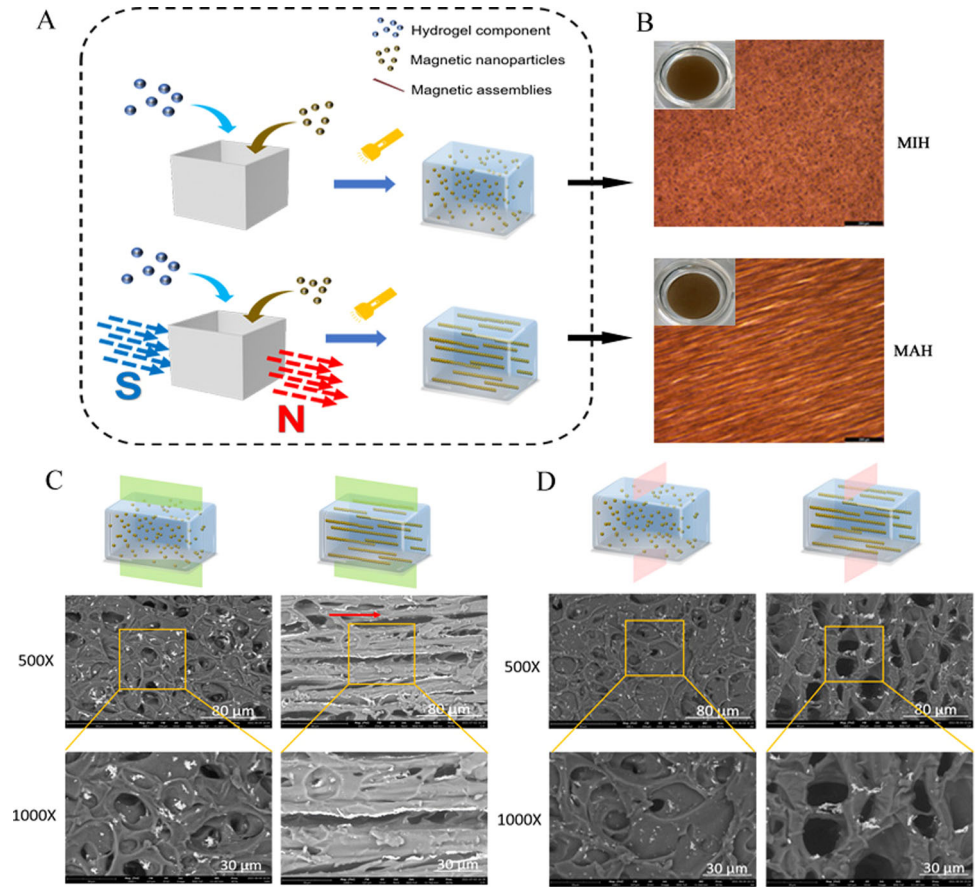

Fig. 1 Morphology of magnetic hydrogels. Schematic illustration of the fabrication procedures for hydrogels with dual anisotropic structures with the assistance of field-induced self-assembly of magnetic nanomaterials (**A**). Macroscopic and microscopy images of MIH and MAH (**B**). Schematic illustration and TEM analysis of cross sections both parallel (**C**) and perpendicular (**D**) to the long axis of the internal assembly structures.

obtained under the two conditions were substantial, and a measurable *g*-factor difference was obtained (0.45), which demonstrated that the MAH had magnetic anisotropy (Fig. 2D–F). Additionally, our research probed the responsiveness of the two magnetic hydrogels to an applied external magnetic field. The evidence suggests that compared with isotropic hydrogels, anisotropic magnetic hydrogels exhibit increased heating, rotation, and movement in the presence of an external magnetic field. A comprehensive summary of these observations is presented in Fig. S3.

Next, a set of standard mechanical tests was performed to quantify the mechanical properties of the MAH. First, the stress-relaxation behavior of these samples was estimated. According to the compression–crack tests (Fig. 2G), the MAH could compress under strain by more than 60% and exhibited a greater loading capacity than the PGH and MIH. Furthermore, this experiment enabled the calculation of the limit compression stress, breaking elongation, and compression modulus for all three groups, which showed that the MAH had enhanced mechanical properties compared to those of the PGH and MIH (Table S1). The results of the strain sweep and frequency sweep tests confirmed the solid-state behavior of the hydrogel. Additionally, the inclusion of nanomaterials increased the stiffness of the hydrogel (Fig. S4). Compression–relaxation cycles showed that hydrogels containing nanomaterials, including the MIH and MAH, exhibited lower energy dissipation than did the pure hydrogel (Fig. 2H). Furthermore, continuous compression–relaxation cycles were performed to evaluate the fast recovery capability of the MAH. The maximum strain and the number of cycles were set to 40% and 5, respectively. After 5 continuous compression–relaxation cycles of the MAH, the relative maximum stress in each cycle barely decreased, indicating that the MAH has excellent rapid recovery ability (Fig. 2I).

Morphology of BMSCs cultured on hydrogels

After 2 days of culture, cell morphology and distribution were observed using an optical microscope and a laser confocal microscope, respectively. Figure 3A shows a

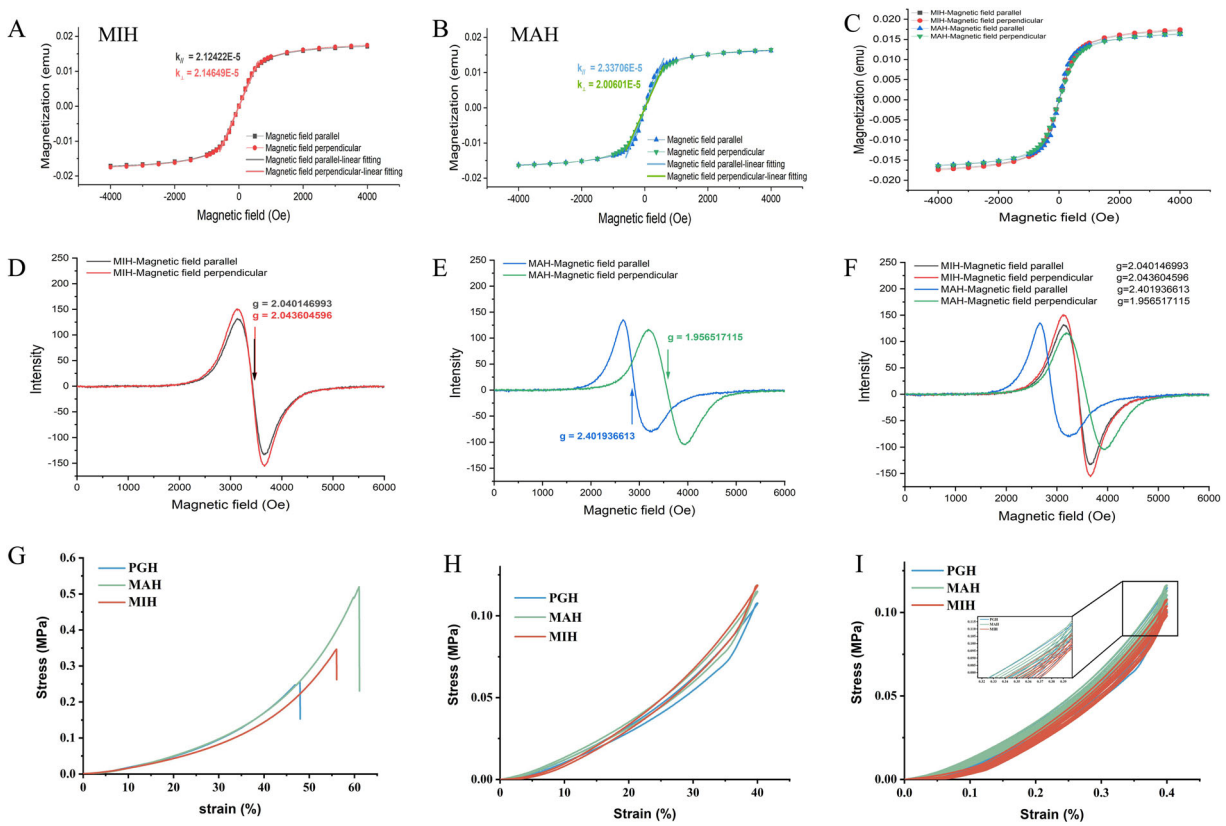

Fig. 2 Magnetic and mechanical properties of the hydrogels. SQUID analysis of the MIH (**A**) and MAH (**B**) was carried out in two orientations: aligned with and perpendicular to the axis of the assembly structure relative to the magnetic field. These data were subsequently summarized (**C**). Similarly, FMR spectroscopy of the MIH (**D**) and MAH (**E**) was carried out in two orientations, and the results are summarized in (**F**). Uniaxial stress–strain curves of PGH, MIH, and MAH under compression until cracking (**G**). Uniaxial compression–relaxation cycles of PGH, MIH, and MAH (**H**). Compression–relaxation cycles of PGH, MIH, and MAH for 5 consecutive cycles without waiting between each cycle (**I**).

schematic illustration of cell seeding and cell adhesion on MAH. BMSCs cultured on PGH (Fig. 3B, E) or MIH (Fig. 3C, F) were stretched and grew in a polygonal pattern. Notably, BMSCs tended to grow along the assembly chain of the magnetic nanomaterials, as shown in the direction of the white arrow in Fig. 3D. The cells were then stained with phalloidin to visualize the cytoskeleton. The polarized structure in the MAH consisted of numerous BMSCs with head-to-tail connections between each single cell (Fig. 3D, G). There was no significant difference in the cytoskeletal structure between the PGH group and the MIH group.

MAH promotes the osteogenic differentiation of BMSCs

To evaluate the osteogenic differentiation of BMSCs cultivated on the PGH, MIH, and MAH, cells were induced with an osteogenic differentiation medium. According to the ALP staining results, the BMSCs on the MAH exhibited increased ALP expression (Fig. 4A). In addition, ALP activity was evaluated on Days 4 and 7. Figure 4B shows that the ALP activity of cells cultured on the MAH was significantly elevated compared to that of cells cultured on the PGH and MIH. Consistently, the MAH substantially upregulated RUNX2 protein expression as differentiation proceeded (Fig. 4C). After 14 days of induction, the BMSCs collected from the MAH expressed the highest levels of several osteogenesis-related genes, including BMP2, COLI, OCN, and ALP, compared to the cells cultured on the other two hydrogels (Fig. 4D–G). The western blot results were consistent with the PCR data (Fig. 4H). Taken together, these data demonstrated that osteogenic differentiation is increased in BMSCs cultured on hydrogels with dual magnetic and topographic anisotropy.

MAH promotes BMSC osteogenesis by upregulating the expression of the lncRNA SNHG5

Recently, numerous studies have reported that lncRNAs are critical for the differentiation of MSCs[38], and substantial changes in lncRNA profiles occur in MSCs during osteogenic differentiation[39]. Therefore, we used RNA-seq to assess the expression of lncRNAs in BMSCs collected

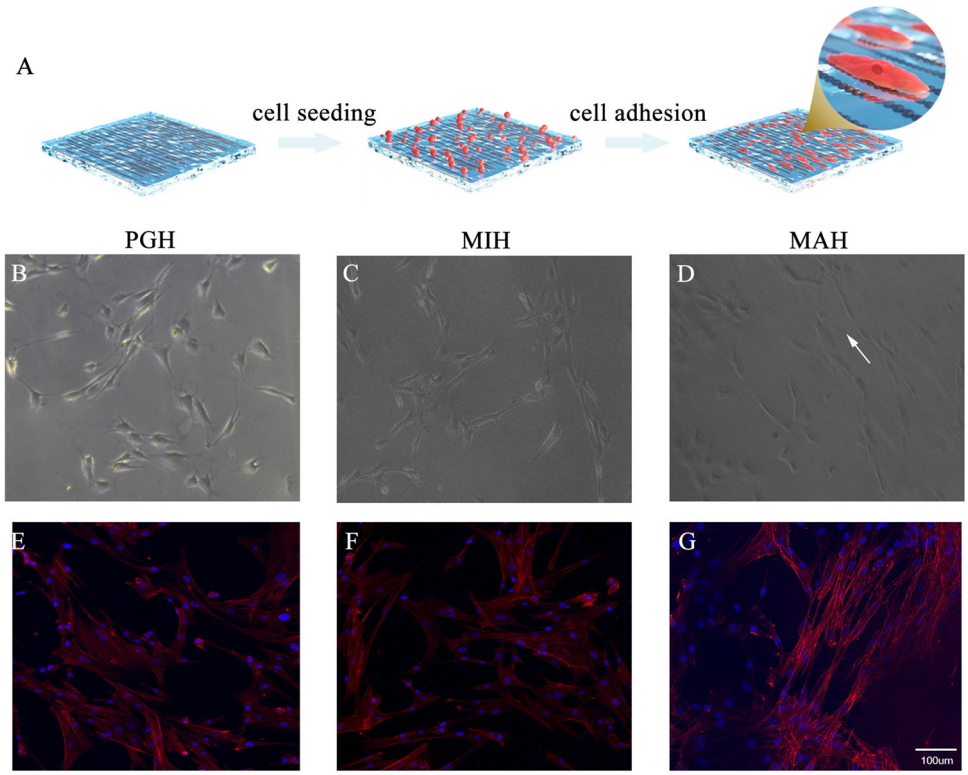

Fig. 3 Morphology of cells cultivated on three different hydrogels. Schematic illustration of cell seeding and cell adhesion on the MAH (**A**). Representative optical microscopy and confocal microscopy images of BMSCs cultivated on PGH (**B**, **E**), MIH (**C**, **F**), and MAH (**D**, **G**) scaffolds. F-actin and nuclei were visualized by rhodamine-phalloidin (red) and DAPI (blue), respectively. BMSCs tended to grow along the assembly chain of the magnetic nanomaterials, as shown by the white arrow.

from the MIH and MAH to determine the effects of these hydrogels' osteogenic differentiation. The expression of lncRNAs in BMSCs significantly differed between the two groups, and the expression level of SNHG5 in BMSCs cultured on the MAH was significantly greater than that in BMSCs cultured on the MIH (Fig. 5A, Table S4). The RNA-seq results were validated by qRT−PCR (Fig. 5B). The expression of SNHG5 significantly increased and peaked on Day 7 in BMSCs cultivated on the MAH (Fig. 5C). We then evaluated the protein-coding potential of SNHG5 using the coding potential calculator (CPC) with ACTA1 (a well-known protein-coding gene) as a protein-coding control and HOTAIR (a classical long noncoding RNA that has been reported to lack protein-coding potential) as a noncoding control. The results revealed that SNHG5 had lower coding potential than HOTAIR (Fig. 5D). Furthermore, to investigate the function of SNHG5 in osteogenic differentiation, we determined the cellular localization of SNHG5 by nuclear/cytoplasmic fractionation and qRT−PCR. We found that SNHG5 was present mostly in the cytoplasm (Fig. 5E, Table S5), which was confirmed by FISH analysis (Fig. 5F).

SNHG5 affects the osteogenic differentiation of BMSCs by activating the NOTCH1 and NOTCH2 signaling pathways via regulation of the miR-32/SIRT6 axis

Numerous studies have revealed that lncRNAs, including some members of the SNHG family[40], act as molecular sponges for miRNAs to regulate the osteogenic differentiation of MSCs[41]. Using bioinformatics analysis and luciferase reporter assays, we found that miR-32 (an anti-osteogenic miRNA[42]) binds to SNHG5 (Fig. S5). In addition, potential binding sites were identified by bioinformatic analyses (Fig. 6A). Moreover, miR-32 significantly decreased the luciferase activity of SNHG5-WT (Fig. 6B), and the RNA pull-down assay demonstrated that SNHG5 was pulled down by miR-32 in BMSCs (Fig. 6C), indicating that SNHG5 is a sponge for miR-32. We next explored the effect of miR-32 on the ability of SNHG5 to promote the osteogenic differentiation of BMSCs. According to qRT−PCR analysis, the expression of miR-32 in BMSCs cultured on the MAH was lower than that in BMSCs cultured on the MIH (Fig. 6D). Pearson's correlation analysis revealed a significant correlation between SNHG5 and miR-32 in BMSCs cultured on the MAH (Fig. 6E).

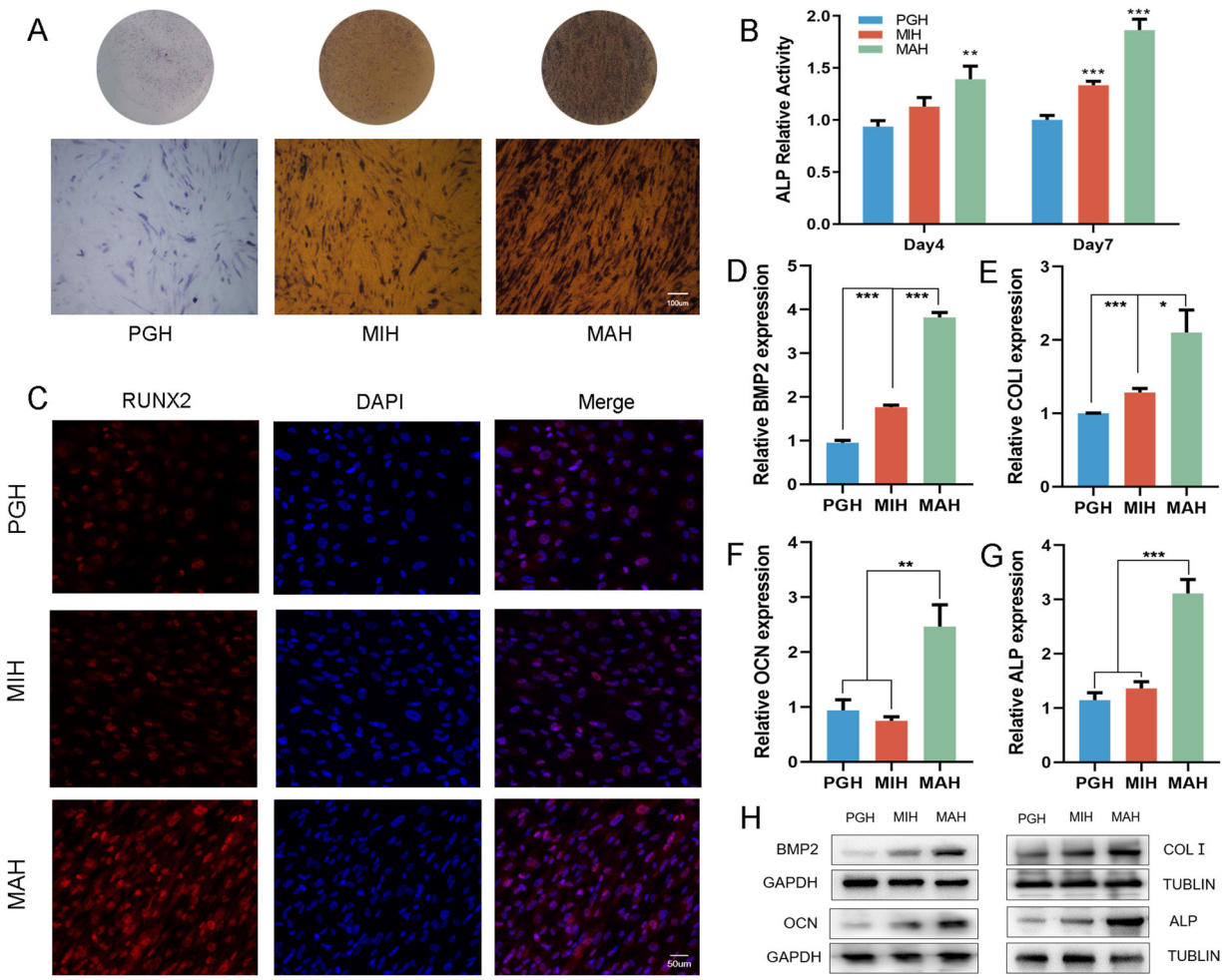

Fig. 4 Osteogenic differentiation of BMSCs cultured on PGH, MIH, and MAH scaffolds. Anisotropic structures generated from magnetic nanomaterial assemblies upregulated osteogenic markers. ALP staining **A** on Day 7 and ALP activity analysis **B** on Days 4 and 7. RUNX2 expression in BMSCs cultivated on PGH, MIH, and MAH scaffolds utilizing RUNX2-specific antibodies (**C**). qRT–PCR analysis of BMP2 (**D**), COLI (**E**), OCN (**F**), and ALP (**G**) in BMSCs after 14 days of culture on PGH, MIH, and MAH scaffolds. Western blot analysis of BMP2, COLI, OCN, and ALP in BMSCs cultivated on the PGH, MIH, and MAH scaffolds (**H**). $^{*}P < 0.05$, $^{**}P < 0.01$, and $^{***}P < 0.001$ (Student's *t* test). The data are presented as the mean ± SD ($n \geq 3$).

To further explore the possible regulatory mechanisms of SNHG5 and miR-32, online bioinformatics tools were used, and SIRT6 was identified as a potential target of miR-32 (Fig. 6F). Moreover, luciferase reporter assays revealed that miR-32 significantly decreased the luciferase activity of SIRT6-WT (Fig. 6G), and qRT−PCR showed that SIRT6 expression in the MAH group was greater than that in the MIH group, and the difference increased with increasing incubation time (Fig. 6H). Pearson's correlation analysis indicated that there was a significant correlation between miR-32 and SIRT6 (Fig. 6I). Western blot analysis showed that sh-SNHG5 downregulated the expression of SIRT6, and this inhibitory effect was partly abolished by miR-32 inhibitors (Fig. 6J). Overall, these results demonstrated that SNHG5 regulates SIRT6 expression by sponging miR-32 during osteogenic differentiation.

SIRT6 has been reported to interact with the NOTCH signaling pathway, which is well known as one of the key signaling pathways involved in osteogenic differentiation and is deactivated by DNMT family-induced hypermethylation[37,43]. Our results verified that NOTCH1 and NOTCH2, but not NOTCH3 or NOTCH4, are potential targets of SIRT6 (Fig. 6K, L). A coimmunoprecipitation assay was subsequently performed, which identified the DNMT1 protein in the SIRT6 protein complex (Fig. 6M). In addition, an immunoprecipitation assay demonstrated that the level of acetylated DNMT1 was significantly lower in SIRT6-overexpressing cells (Fig. 6N), indicating that SIRT6 partially suppresses the abnormal DNA methylation of NOTCH1 and NOTCH2 by antagonizing DNMT1 through protein deacetylation. Taken together, these results demonstrated that the MAH regulates the

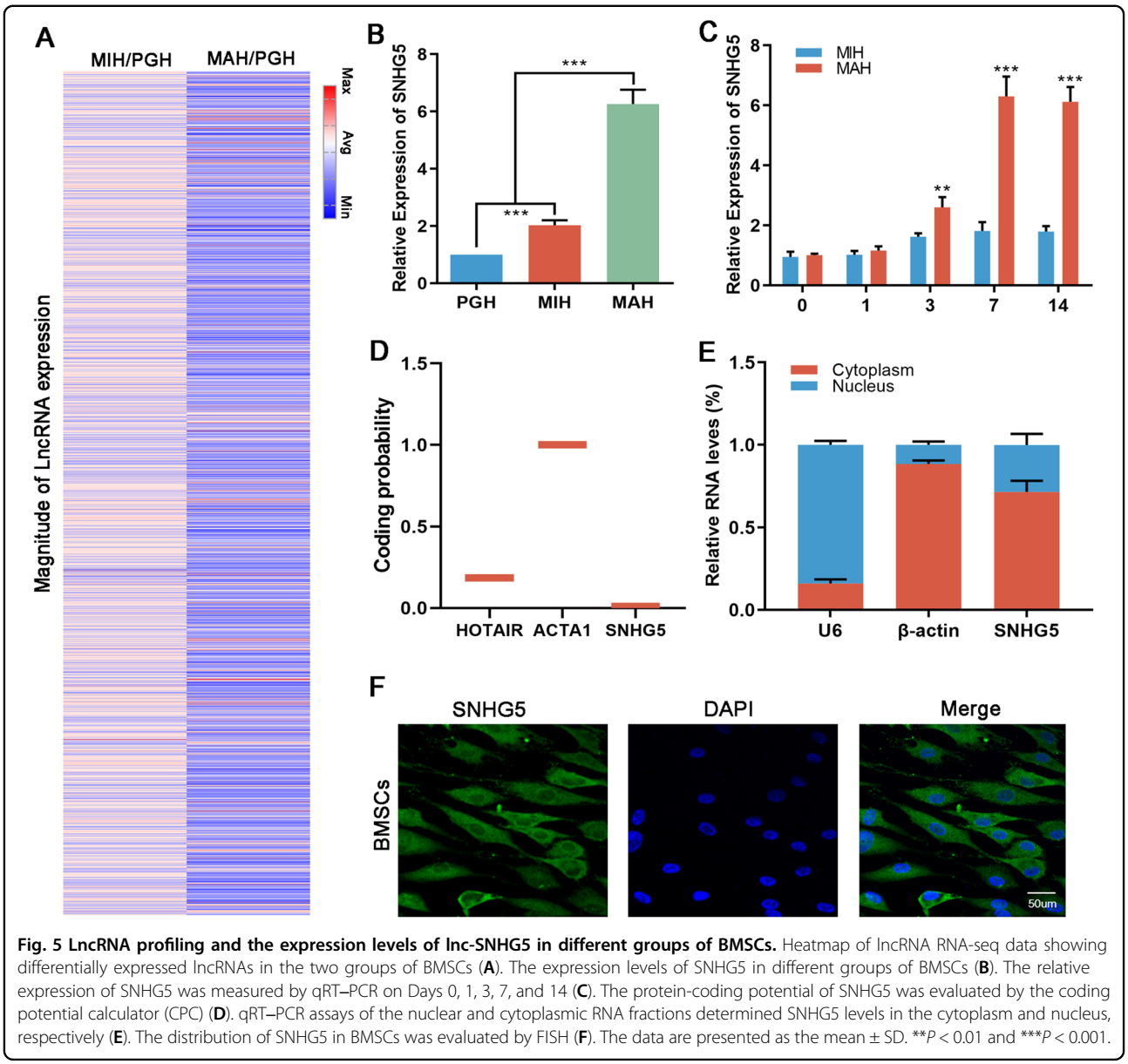

Fig. 5 LncRNA profiling and the expression levels of lnc-SNHG5 in different groups of BMSCs. Heatmap of lncRNA RNA-seq data showing differentially expressed lncRNAs in the two groups of BMSCs (**A**). The expression levels of SNHG5 in different groups of BMSCs (**B**). The relative expression of SNHG5 was measured by qRT–PCR on Days 0, 1, 3, 7, and 14 (**C**). The protein-coding potential of SNHG5 was evaluated by the coding potential calculator (CPC) (**D**). qRT–PCR assays of the nuclear and cytoplasmic RNA fractions determined SNHG5 levels in the cytoplasm and nucleus, respectively (**E**). The distribution of SNHG5 in BMSCs was evaluated by FISH (**F**). The data are presented as the mean ± SD. $^{**}P < 0.01$ and $^{***}P < 0.001$.

osteogenic differentiation of BMSCs by modulating the NOTCH1 and NOTCH2 pathways via posttranslational modification through SNHG5/miR-32/SIRT6 DNMT1 signaling. Figure 7 shows a diagram of the detailed mechanism.

Bone regeneration evaluation

In vitro studies confirmed that the MAH demonstrated superior biocompatibility, mechanical robustness, and elevated osteogenic potential. This led us to probe the in vivo bone regeneration capacities of the developed hydrogels. Accordingly, all three hydrogel groups were assessed using a rabbit femoral defect model. In the control scenario, no subsequent procedures were carried out after defect induction (as depicted in Fig. S6). At 2-month intervals post-implantation, femurs were extracted and initially evaluated via micro-CT. The 3D reconstructions and cross-sectional views in Fig. 8B show a pronounced defect in the control group, and the MAH-treated group had more newly formed bone than the PGH group. Key metrics such as BV/TV and BS/TV, as well as trabecular attributes such as Tb.Th, Tb.Sp, and Tb.N, were quantitatively measured, and the results are shown in Fig. 8C. In the control group, the BV/TV ratio was 0.2498 ± 0.0671. The MAH group exhibited a BV/TV of 0.5970 ± 0.0374, which also exceeded the values obtained for the PGH and MIH groups. A consistent trend was observed in the BS/TV. In terms of trabecular

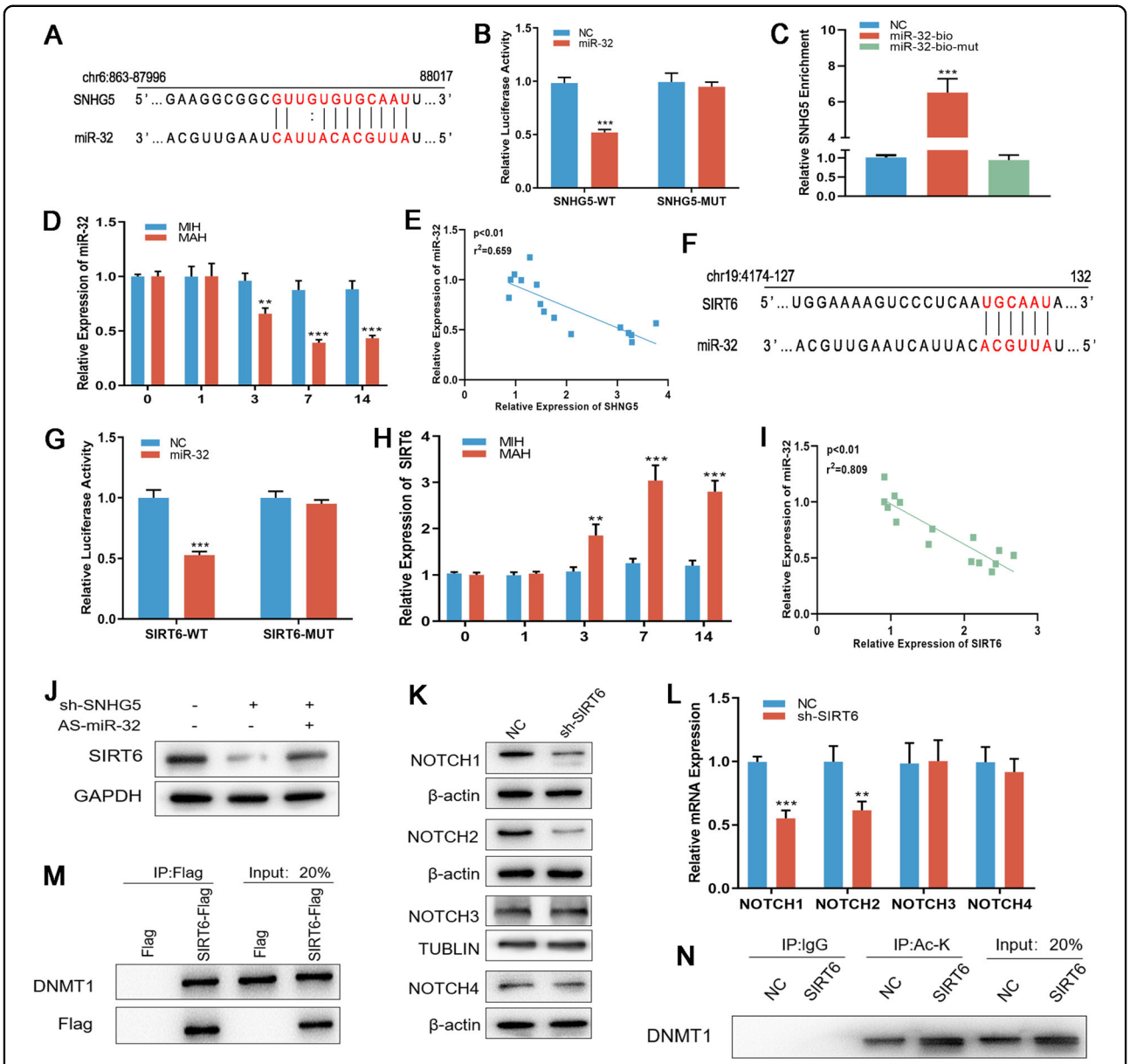

Fig. 6 SNHG5 functions as a molecular sponge for miR-32 and regulates the expression of SIRT6 during osteogenic differentiation by modulating the biological effects of SIRT6-related downstream signal transduction pathways. Potential targeted binding between SNHG5 and miR-32 (**A**). The identified complementary binding sites were validated by dual-luciferase reporter and RNA pull-down assays (**B**, **C**). The relative expression of miR-32 was measured by qRT–PCR at Days 0, 1, 3, 7, and 14 (**D**). Pearson's correlation analysis of SNHG5 and miR-32 in cells grown on MAH scaffolds (**E**). The putative binding sites of miR-32 on SIRT6 were predicted via an online database (**F**). A luciferase reporter assay indicated that miR-32 reduced the luciferase activity of SIRT6 (**G**). The relative expression of SIRT6 was measured by qRT–PCR on Days 0, 1, 3, 7, and 14 (**H**). Pearson's correlation analysis of miR-32 and SIRT6 expression in the cells grown on MAH scaffolds (**I**). Western blot analyses of SIRT6 expression in BMSCs transfected with NC, si-SNHG5, or si-SNHG5 together with the miR-32 inhibitor (**J**). Western blot and qRT–PCR analyses showed that the expression of NOTCH1 and NOTCH2 was decreased by SIRT6 knockdown (**K**, **L**). IP analysis was performed in Flag-SIRT6-overexpressing BMSCs (**M**). IP analysis was performed with an acetylated lysine (Ac-K) antibody using Flag-SIRT6-overexpressing BMSC nuclear extracts, and DNMT1 protein levels in the Ac-K IP were evaluated via western blot analysis (**N**). The data are presented as the mean ± SD. $^{**}P < 0.01$ and $^{***}P < 0.001$.

characteristics, Tb.N and Tb.Th was significantly greater after treatment with the MAH than in the other groups, while Tb.Sp was significantly lower (Fig. 8C). These results confirmed that the MAH accelerates bone regeneration in vivo. Similar trends were observed in the Masson and H&E staining results (Fig. 8D). In summary, MAH clearly possesses an outstanding capacity to expedite bone tissue regeneration.

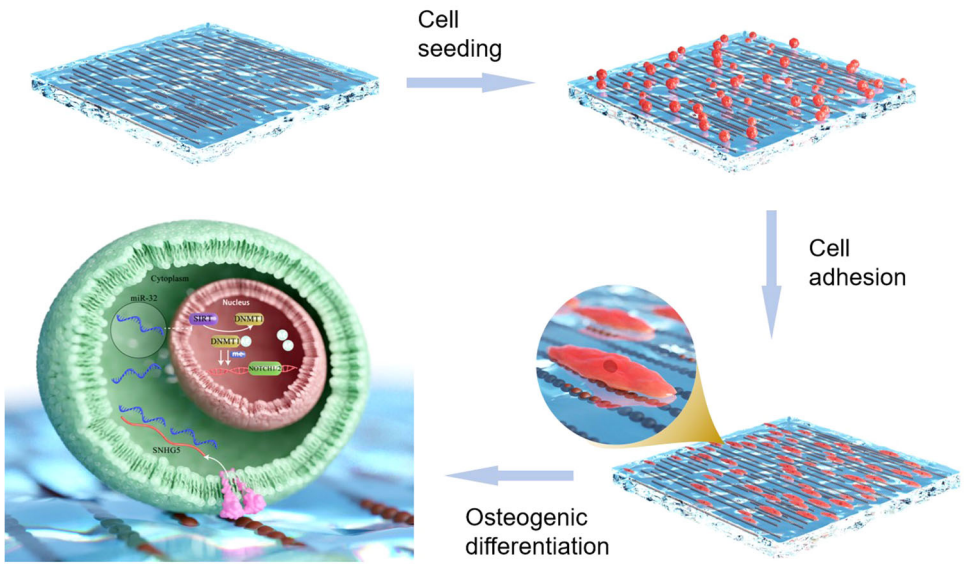

Fig. 7 Proposed mechanism of MAH-induced osteogenic differentiation of BMSCs.

Discussion

The scaffold is one of the crucial elements in bone tissue engineering. Increasing the osteoinductive capability of scaffolds has persistently been a topic of keen interest and a widely pursued challenge. An increasing emphasis on design principles obtained from the basic mechanisms of cell–matrix interactions and cell signaling has now set the stage for the successful application of biomaterials in cell-based bone tissue engineering[44]. In the extracellular microenvironment, physical factors significantly influence stem cell differentiation. The use of these factors is now a novel approach for designing bone tissue engineering scaffolds. Notably, scaffolds with multiscale anisotropy exhibit biomimetic attributes, which increase their biofunctionality. The isotropic nature of many commonly used scaffolds is markedly different from the inherent anisotropic tendencies of bone. Enriching scaffold designs with composite materials to introduce anisotropy can increase biomimicry and osteogenic reactivity, marking a paradigm shift in bone scaffolding. Recently, MNMs have been reported to have great potential for use in controlling cell fate and investigating cell mechanotransduction in bone tissue engineering[45,46]. In our previous research, we fabricated anisotropic structures on a polydimethylsiloxane (PDMS) substrate via magnetic nanomaterial assembly and verified that the resulting structures promoted the osteogenic differentiation of MSCs. However, owing to the high viscosity of the PDMS monomer and preparation process, we could assemble MNMs only on the surface of the PDMS, resulting in limited magnetic anisotropy. Moreover, the slow degradation of PDMS and the production of acid during the degradation process can cause inflammatory reactions in the surrounding tissues, leading to poor osteoinductivity and introducing limitations in in vivo application[33]. Similarly, most magnetic composite scaffolds have MNMs on the surface of the scaffold, from which they are easily dislodged, rendering the assembled structures sensitive to friction during bone tissue regeneration. These factors reduce the efficiency of osteogenic induction and fail to maximize the magnetic biological effects of MNMs. Therefore, a biocompatible matrix material capable of massive and homogeneous assembly of MNMs is a promising candidate for study.

Herein, an MAH was designed by combining MNMs and a PEGDA–GelMA hydrogel with the assistance of a static magnetic field, and the MAH was then sliced parallel to the assembly direction of the MNMs, producing a structure that has been shown to promote the osteogenic differentiation of BMSCs. Many studies have confirmed that mechanical stretching plays a crucial role in the osteogenic differentiation of MSCs[47]. In our MAH, numerous assemblies were exposed to the surface after slicing, which allowed the inoculated cells to interact with the exposed assemblies and stretch in this direction. The hydrogels were sliced before being used as a cell culture matrix, and the roughness of the sliced surface was characterized in our previous study and shown to be outside the range that affected the behavior of cells[48]. Sections cut parallel and sections cut perpendicular to the assembly direction revealed that the polymer matrix of the hydrogel formed under magnetic influence aligns with the nanoassembly orientation. This is likely due to the alignment of the system's magnetic nanomaterials in

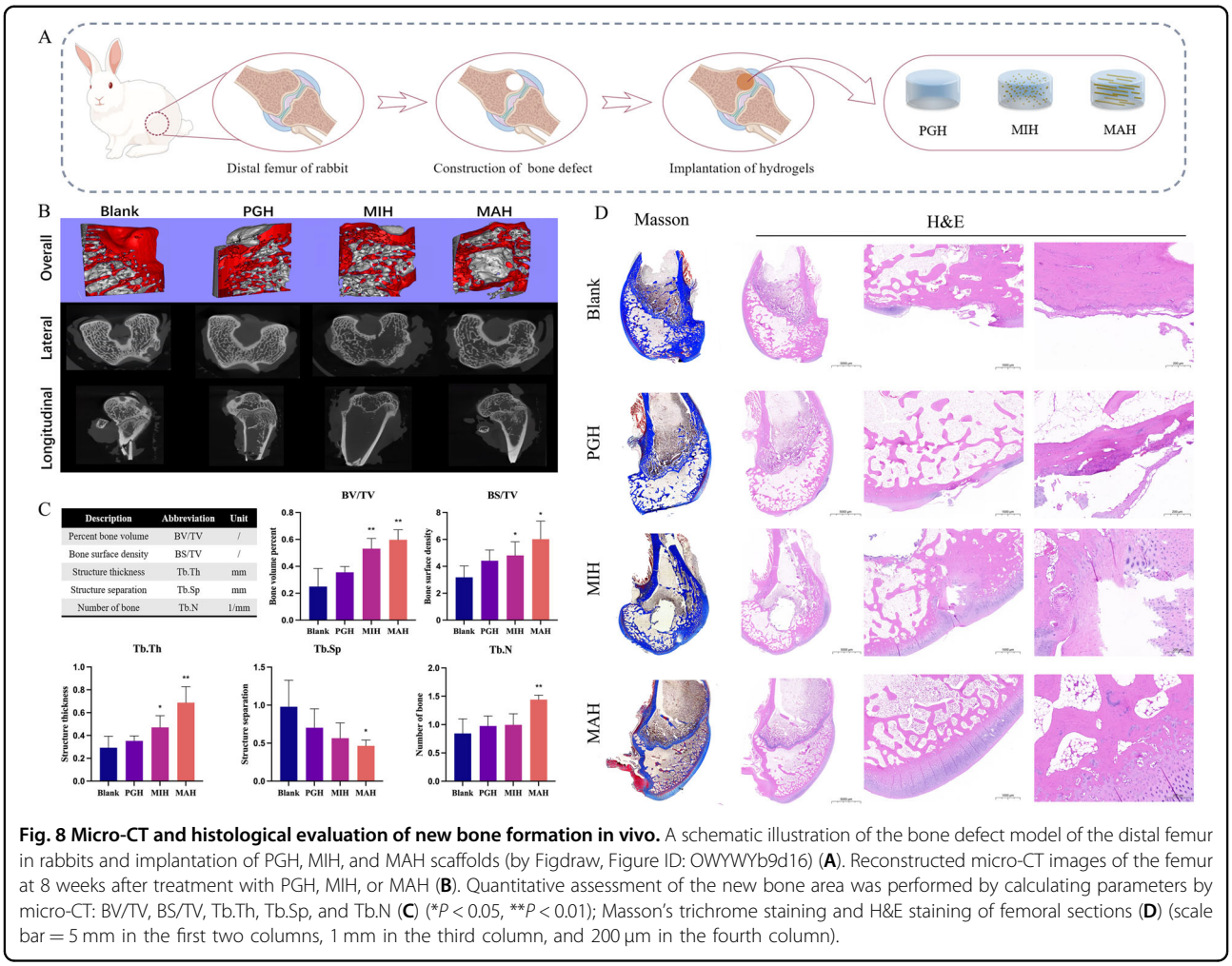

Fig. 8 Micro-CT and histological evaluation of new bone formation in vivo. A schematic illustration of the bone defect model of the distal femur in rabbits and implantation of PGH, MIH, and MAH scaffolds (by Figdraw, Figure ID: OWYWYb9d16) (**A**). Reconstructed micro-CT images of the femur at 8 weeks after treatment with PGH, MIH, or MAH (**B**). Quantitative assessment of the new bone area was performed by calculating parameters by micro-CT: BV/TV, BS/TV, Tb.Th, Tb.Sp, and Tb.N (**C**) (*$P < 0.05$, **$P < 0.01$); Masson's trichrome staining and H&E staining of femoral sections (**D**) (scale bar = 5 mm in the first two columns, 1 mm in the third column, and 200 μm in the fourth column).

response to the external magnetic field as the hydrogel solidifies. These nanomaterials serve as templates during the crosslinking process, prompting similar alignment of the gel monomers. Furthermore, this unique polymer configuration bolsters the stability of the nanoassembly during its formation and solidification, leading to a composite hydrogel characterized by dual topographic and magnetic anisotropy. Moreover, increasing evidence indicates that magnetic fields and magnetically responsive scaffolds play unique roles in promoting bone repair and regeneration[17]. In the present study, FMR spectroscopy and SQUID results showed that the magnetic property of the MAH was stronger in the direction parallel to the assemblies than in the direction perpendicular to them, which provided cells with an oriented micromagnetic field. In contrast to scaffolds with only surface-assembled MNMs, the MAH exhibited a relatively homogeneous internal assembly structure. This was attributed to the assembly of nanomaterials in the magnetic hydrogel occurring in the liquid phase, in contrast to the interfacial assembly process, in which the nanomaterials are affected by random isotropic perturbations caused by the evaporation process. Because the exposed surface assemblies were also partially embedded in the hydrogel, the efficacy of the assembly structure was not affected by cell contact or liquid immersion[49]. With the degradation of the scaffold, the MNMs are gradually released into the defect site, which is also thought to promote the osteogenic differentiation of stem cells. A series of in vitro experiments, including qRT−PCR, WB, ALP detection, and IF staining, demonstrated that the MAH significantly promoted the induction of osteogenic differentiation in BMSCs.

Although we demonstrated the promising osteogenic effects of the MAH, further investigations remain necessary to clarify the regulatory mechanism involved and provide a theoretical guide for the future design of bone tissue engineering. Recently, lncRNAs have been reported to play vital roles in the osteogenic differentiation of MSCs[50]. To investigate the mechanism of MAH-induced osteogenesis in BMSCs, RNA-seq was performed, and the results demonstrated that the expression of the lncRNA SNHG5 was significantly changed. Osteogenesis-related

lncRNAs have been reported to have different cellular localizations and molecular mechanisms[51]. We found that SNHG5 was present mainly in the cytoplasm and functioned as a microRNA (miR-32) sponge. Recent studies have revealed that miR-32 performs important functions in osteogenic differentiation[42], but its mechanism has not yet been elucidated. As miRNAs function by regulating their target genes[52], we predicted potential target genes by bioinformatics analysis and confirmed that miR-32 targets SIRT6. SIRTs are NAD1-dependent deacetylases that are involved in MSC differentiation[53]. In the present study, we demonstrated that SIRT6 promoted osteogenic differentiation by modifying NOTCH1/2 signaling but not NOTCH3/4 signaling. Previous studies[54] have reported that DNMT1 participates in the regulation of DNA methylation in NOTCH. Herein, we demonstrated that the SIRT6 protein deacetylated and destabilized the DNMT1 protein via physical interaction, which regulated the DNA methylation status of NOTCH1/2. The present study revealed for the first time that MAH-enhanced BMSC osteogenesis is partly controlled by a novel molecular network consisting of SNHG5, miR-32, SIRT6, DNMT1, and NOTCH1/2. In summary, the MAH might affect the osteogenic differentiation of BMSCs through the SNHG5/miR-32 regulatory axis, which regulates the DNA methylation status of NOTCH1/2 via the SIRT6–DNMT1 complex. These results demonstrated the role of magnetic and anisotropic conditioning in defining stem cell osteogenic differentiation pathways and optimizing the induction of terminal osteogenesis utilizing a combination of magnetic and topographic conditioning. In addition, these data provide useful insight into the modality and mechanism of the MAH-induced osteogenic differentiation of BMSCs.

Conclusion

In the present study, a nanocomposite hydrogel with magnetic and topographic anisotropy was fabricated via the combination of a PEGDA–GelMA hydrogel and field-induced magnetic nanomaterials. The interaction between dual anisotropic properties and BMSCs leads to osteogenic gene responses that induce the osteogenic differentiation of BMSCs. In addition, our results suggested a novel underlying MAH-induced osteogenic mechanism involving SNHG5/miR-32/SIRT6/DNMT1/NOTCH signaling. In vivo studies confirmed that the dual anisotropic hydrogel strongly promoted bone regeneration. These results suggest a new strategy for optimizing the design of bone tissue engineering scaffolds.

Acknowledgements
This work was supported by grants from the National Key Research and Development Project (2021YFA1201302, 2016YFA0201704) and the National Natural Science Foundation of China (81870807, 81701824, and 51832001).

Author details
[1]Jiangsu Province Key Laboratory of Oral Diseases, Nanjing Medical University, 210029 Nanjing, China. [2]Department of Prosthodontics, Affiliated Stomatological Hospital of Nanjing Medical University, 210029 Nanjing, China. [3]Jiangsu Province Engineering Research Center of Stomatological Translational Medicine, 210029 Nanjing, China. [4]Division of Sports Medicine and Adult Reconstructive Surgery, Department of Orthopedic Surgery, Nanjing Drum Tower Hospital, Affiliated Hospital of Medical School, Nanjing University, 321 Zhongshan Road, 210008 Nanjing, China. [5]Nanjing Stomatological Hospital, Affiliated Hospital of Medical School, Nanjing University, 210008 Nanjing, China. [6]Key Laboratory for Bio-Electromagnetic Environment and Advanced Medical Theranostics, School of Biomedical Engineering and Informatics, Nanjing Medical University, 211166 Nanjing, China. [7]Cardiovascular Disease Research Center, Nanjing Drum Tower Hospital, Affiliated Hospital of Medical School, Medical School, Nanjing University, 210093 Nanjing, China. [8]Shanghai Frontiers Science Center of TCM Chemical Biology, Institute of Interdisciplinary Integrative Medicine Research, Shanghai University of Traditional Chinese Medicine, 201203 Shanghai, China

Author contributions
S.T.: Conceptualization, methodology, data curation, formal analysis, writing—original draft. Y.Y. and P.W.: Animal experiment implementation, formal analysis. X.-L.L.: Data curation, investigation, and methodology. X.-Q.X.: Resources and investigation. K.H.: Methodology. S.Y.: Conceptualization and methodology. Z.-B.G.: Writing—review and editing. X.H.: conceptualization and methodology. F.Z.: Conceptualization, funding acquisition, and supervision. N.G.: Supervision.

Conflict of interest
The authors declare no competing interests.

Supplementary information The online version contains supplementary material available at https://doi.org/10.1038/s41427-024-00535-x.

Received: 11 October 2023 Revised: 20 January 2024 Accepted: 25 January 2024
Published online: 22 March 2024

References

1. Kim, H. N. et al. Nanotopography-guided tissue engineering and regenerative medicine. *Adv. Drug Deliv. Rev.* **65**, 536–558 (2013).
2. Davis, H. E., Case, E. M., Miller, S. L., Genetos, D. C. & Leach, J. K. Osteogenic response to BMP-2 of hMSCs grown on apatite-coated scaffolds. *Biotechnol. Bioeng.* **108**, 2727–2735 (2011).
3. Kim, J. et al. Synergistic effects of nanotopography and co-culture with endothelial cells on osteogenesis of mesenchymal stem cells. *Biomaterials* **34**, 7257–7268 (2013).
4. Hiew, V. V., Simat, S. F. B. & Teoh, P. L. The advancement of biomaterials in regulating stem cell fate. *Stem Cell Rev. Rep.* **14**, 43–57 (2018).
5. Kim, D. H., Provenzano, P. P., Smith, C. L. & Levchenko, A. Matrix nanotopography as a regulator of cell function. *J. Cell Biol.* **197**, 351–360 (2012).
6. Chu, G. et al. Substrate stiffness- and topography-dependent differentiation of annulus fibrosus-derived stem cells is regulated by Yes-associated protein. *Acta Biomater.* **92**, 254–264 (2019).
7. Jang, W. G., Kim, E. J., Lee, K. N., Son, H. J. & Koh, J. T. AMP-activated protein kinase (AMPK) positively regulates osteoblast differentiation via induction of Dlx5-dependent Runx2 expression in MC3T3E1 cells. *Biochem. Biophys. Res. Commun.* **404**, 1004–1009 (2011).
8. Hu, Q., Liu, M., Chen, G., Xu, Z. & Lv, Y. Demineralized bone scaffolds with tunable matrix stiffness for efficient bone integration. *ACS Appl. Mater. Interfaces* **10**, 27669–27680 (2018).
9. Wang, S. et al. A high-strength mineralized collagen bone scaffold for large-sized cranial bone defect repair in sheep. *Regen. Biomater.* **5**, 283–292 (2018).

10. Yu, L. et al. Biomimetic bone regeneration using angle-ply collagen membrane-supported cell sheets subjected to mechanical conditioning. *Acta Biomater.* **112**, 75–86 (2020).
11. Cartmell, S. H., Dobson, J., Verschueren, S. B. & El Haj, A. J. Development of magnetic particle techniques for long-term culture of bone cells with intermittent mechanical activation. *IEEE Trans. Nanobiosci.* **1**, 92–97 (2002).
12. Ledda, M. et al. Biocompatibility assessment of sub-5 nm silica-coated superparamagnetic iron oxide nanoparticles in human stem cells and in mice for potential application in nanomedicine. *Nanoscale* **12**, 1759–1778 (2020).
13. Zhang, X., Zhang, Y., Zhang, W., Dai, Y. & Xia, F. Gold nanoparticles-deranged double network for Janus adhesive-tough hydrogel as strain sensor. *Chem. Eng. J.* **420**, 130447 (2021).
14. Lin, S. et al. Gold nanorods crosslinking PNIPAM hydrogels via dynamic Au-thiolate interaction with stretchable, adhesive, self-healing, and photothermal properties. *Gold Bull.* **54**, 59−67 (2021).
15. Jiang, S., Wang, K., Dai, Y., Zhang, X. & Xia, F. Near-infrared light-triggered dual drug release using gold nanorod-embedded thermosensitive nanogel-cross-linked hydrogels. *Macromol. Mater. Eng.* **304**, 1900087 (2019).
16. Pommerenke, H. et al. The mode of mechanical integrin stressing controls intracellular signaling in osteoblasts. *J. Bone Mineral Res.* **17**, 603–611 (2002).
17. Zhao, Y. Z. et al. Magnetic PLGA microspheres loaded with SPIONs promoted the reconstruction of bone defects through regulating the bone mesenchymal stem cells under an external magnetic field. *Mater. Sci. Eng. C Mater. Biol. Appl.* **122**, 111877 (2021).
18. Calabrese, G. et al. Au, Pd and maghemite nanofunctionalized hydroxyapatite scaffolds for bone regeneration. *Regen. Biomater.* **7**, 461–469 (2020).
19. Singh, D., McMillan, J. M., Kabanov, A. V., Sokolsky-Papkov, M. & Gendelman, H. E. Bench-to-bedside translation of magnetic nanoparticles. *Nanomedicine* **9**, 501–516 (2014).
20. Lin, T. C., Lin, F. H. & Lin, J. C. In vitro feasibility study of the use of a magnetic electrospun chitosan nanofiber composite for hyperthermia treatment of tumor cells. *Acta Biomater.* **8**, 2704–2711 (2012).
21. Shao, S. et al. Nanofiltration membranes with crumpled polyamide films: a critical review on mechanisms, performances, and environmental applications. *Environ. Sci. Technol.* **56**, 12811–12827 (2022).
22. Zhao, Z., Fang, R., Rong, Q. & Liu, M. Bioinspired nanocomposite hydrogels with highly ordered structures. *Adv. Mater.* **29**, 1703045 (2017).
23. Matsugaki, A., Fujiwara, N. & Nakano, T. Continuous cyclic stretch induces osteoblast alignment and formation of anisotropic collagen fiber matrix. *Acta Biomater.* **9**, 7227–7235 (2013).
24. Chen, H. et al. Enhanced osteogenesis of ADSCs by the synergistic effect of aligned fibers containing collagen I. *ACS Appl. Mater. Interfaces* **8**, 29289–29297 (2016).
25. You, F. et al. Fabrication and Osteogenesis of a porous nanohydroxyapatite/polyamide scaffold with an anisotropic architecture. *ACS Biomater. Sci. Eng.* **1**, 825–833 (2015).
26. Li, J. et al. Bone regeneration and infiltration of an anisotropic composite scaffold: an experimental study of rabbit cranial defect repair. *J. Biomater. Sci. Polym. Ed.* **27**, 327–338 (2016).
27. Della Sala, F. et al. Mechanical behavior of bioactive poly(ethylene glycol) diacrylate matrices for biomedical application. *J. Mech. Behav. Biomed. Mater.* **110**, 103885 (2020).
28. Shen, J., Dai, Y., Xia, F. & Zhang, X. Polyacrylamide/EDTA-modified chitosan/graphene oxide hydrogels as an adsorbent and supercapacitor for sustainable applications. *Sustain. Mater. Technol.* **36**, e00586 (2023).
29. Zhang, Y. et al. Nanocomposite adhesive hydrogels: from design to application. *J. Mater. Chem. B* **9**, 585–593 (2021).
30. Ma, L. et al. Biomimetic Ti–6Al–4V alloy/gelatin methacrylate hybrid scaffold with enhanced osteogenic and angiogenic capabilities for large bone defect restoration. *Bioact. Mater.* **6**, 3437–3448 (2021).
31. Yuan, Z. et al. Injectable GelMA cryogel microspheres for modularized cell delivery and potential vascularized bone regeneration. *Small* **17**, e2006596 (2021).
32. Li, X. et al. Hydrogel composites with different dimensional nanoparticles for bone regeneration. *Macromol. Rapid Commun.* **42**, e2100362 (2021).
33. Hu, K. et al. Dual anisotropicity comprising 3D printed structures and magnetic nanoparticle assemblies: towards the promotion of mesenchymal stem cell osteogenic differentiation. *NPG Asia Mater.* **13**, 19 (2021).
34. Li, L. et al. The triply periodic minimal surface-based 3D printed engineering scaffold for meniscus function reconstruction. *Biomater. Res.* **26**, 45 (2022).
35. Tang, S. et al. High quality multicellular tumor spheroid induction platform based on anisotropic magnetic hydrogel. *ACS Appl. Mater. Interfaces* **9**, 10446–10452 (2017).
36. Liu, L. et al. The COX10-AS1/miR-641/E2F6 feedback loop is involved in the progression of glioma. *Front. Oncol.* **11**, 648152 (2021).
37. Jia, B. et al. SIRT6 promotes osteogenic differentiation of adipose-derived mesenchymal stem cells through antagonizing DNMT1. *Front. Cell Dev. Biol.* **9**, 648627 (2021).
38. Ju, C. et al. Mesenchymal stem cell-associated lncRNA in osteogenic differentiation. *Biomed. Pharmacother.* **115**, 108912 (2019).
39. Tang, S. et al. LncRNA-OG promotes the osteogenic differentiation of bone marrow-derived mesenchymal stem cells under the regulation of hnRNPK. *Stem Cells* **37**, 270–283 (2019).
40. Liu, Z. H. et al. LncRNA SNHG14 promotes osteogenic differentiation of human bone marrow-derived mesenchymal stem cells via regulating miR-185-5p/WISP2 axis. *J. Biol. Regul. Homeost. Agents* **35**, 605–615 (2021).
41. Ye, G. et al. IRF2-mediated upregulation of lncRNA HHAS1 facilitates the osteogenic differentiation of bone marrow-derived mesenchymal stem cells by acting as a competing endogenous RNA. *Clin. Transl. Med.* **11**, e429 (2021).
42. Zhai, M., Zhu, Y., Yang, M. & Mao, C. Human mesenchymal stem cell derived exosomes enhance cell-free bone regeneration by altering their miRNAs profiles. *Adv. Sci.* **7**, 2001334 (2020).
43. Thomas, S. & Jaganathan, B. G. Signaling network regulating osteogenesis in mesenchymal stem cells.*J. Cell Commun. Signal.* **16**, 47–61 (2022).
44. Lutolf, M. P., Gilbert, P. M. & Blau, H. M. Designing materials to direct stem-cell fate. *Nature* **462**, 433–441 (2009).
45. Xia, Y. et al. Magnetic field and nano-scaffolds with stem cells to enhance bone regeneration. *Biomaterials* **183**, 151–170 (2018).
46. Wang, Q. et al. Response of MAPK pathway to iron oxide nanoparticles in vitro treatment promotes osteogenic differentiation of hBMSCs. *Biomaterials* **86**, 11–20 (2016).
47. Xi, X. et al. Nrf2 activation is involved in osteogenic differentiation of periodontal ligament stem cells under cyclic mechanical stretch. *Exp. Cell Res.* **403**, 112598 (2021).
48. Hu, K. et al. Sliced magnetic polyacrylamide hydrogel with cell-adhesive microarray interface: a novel multicellular spheroid culturing platform. *ACS Appl. Mater. Interfaces* **8**, 15113–15119 (2016).
49. Guo, Z. et al. Fabrication of hydrogel with cell adhesive micropatterns for mimicking the oriented tumor-associated extracellular matrix. *ACS Appl. Mater. Interfaces* **6**, 10963–10968 (2014).
50. He, S. et al. LncRNA ODIR1 inhibits osteogenic differentiation of hUC-MSCs through the FBXO25/H2BK120ub/H3K4me3/OSX axis. *Cell Death Dis.* **10**, 947 (2019).
51. Li, Z. et al. LncRNA H19 promotes the committed differentiation of stem cells from apical papilla via miR-141/SPAG9 pathway. *Cell Death Dis.* **10**, 130 (2019).
52. Li, Q., Hu, Z., Rong, X., Chang, B. & Liu, X. Multifunctional polyplex micelles for efficient microRNA delivery and accelerated osteogenesis. *Nanoscale* **13**, 12198–12211 (2021).
53. Zheng, K. et al. Protective effects of sirtuin 3 on titanium particle-induced osteogenic inhibition by regulating the NLRP3 inflammasome via the GSK-3beta/beta-catenin signalling pathway. *Bioact. Mater.* **6**, 3343–3357 (2021).
54. Yan, J. et al. Diabetes impairs wound healing by Dnmt1-dependent dysregulation of hematopoietic stem cells differentiation towards macrophages. *Nat. Commun.* **9**, 33 (2018).